

# Quantifying the global impact of tropical cyclone-associated gravity waves using HIRDLS, MLS, SABER and IBTrACS data

Corwin J. Wright

Centre for Space, Atmospheric and Oceanic Science, University of Bath, Bath, UK

## Correspondence

Corwin Wright, Centre for Space, Atmospheric and Oceanic Science, University of Bath, Bath BA2 7AY, UK.  
Email: c.wright@bath.ac.uk

## Funding information

Royal Society University Research Fellowship UF160545; Natural Environment Research Council Grant NE/R001391/1;

## Abstract

Tropical convective systems are major sources of atmospheric gravity waves (GWs). These waves are a key driver of global atmospheric circulation, especially in the middle and upper atmosphere. Tropical cyclones (TCs) such as hurricanes and typhoons are particularly dramatic examples of such systems, and are therefore potentially significant individual sources of GWs. To investigate this effect, GW observations from three satellite limb sounders in the vicinity of TCs are produced and analysed. By statistically combining 15 years of GW observations from 1,379 individual TCs represented in the International Best Track Archive for Climate Stewardship, it is shown that TCs are associated with a 15% increase of GW amplitudes over background and a 25% increase in measured momentum fluxes, primarily during the period immediately before the TC. It is further shown that this additional contribution is small relative to other GW-generating processes, and thus that individual TCs do not have a large quantitative effect on the dynamics of the middle and upper atmosphere as a whole. Thus, it is concluded that accurate modelling of TC-generated short vertical wavelength GWs need not be a development priority for the next generation of weather and climate models. The results also demonstrate that stronger GW activity is associated with TCs that will later develop into hurricane-intensity storms than is observed for those that will not, and thus that better space-based monitoring of stratospheric GW activity could be a useful tool to help improve the forecasting of strong hurricane events in the presence of obscuring tropospheric cloud.

## KEY WORDS

gravity waves, mesosphere, remote sensing, satellites, stratosphere, tropical cyclones

## 1 | INTRODUCTION

Gravity waves (GWs) are atmospheric waves that transport energy and momentum, coupling and connecting the different atmospheric layers. They are a key driving factor in the atmospheric flow at all altitudes above the troposphere. Understanding and properly characterising GWs is

thus vital for both numerical weather prediction and climate modelling.

GWs are generated by various geophysical processes, primarily but not exclusively at the surface and in the troposphere. These processes include wind flow over mountains (“orographic” generation) and a range of other mechanisms including jet stream instabilities, weather

This is an open access article under the terms of the Creative Commons Attribution License, which permits use, distribution and reproduction in any medium, provided the original work is properly cited.

© 2019 The Authors. *Quarterly Journal of the Royal Meteorological Society* published by John Wiley & Sons Ltd on behalf of the Royal Meteorological Society.

systems and convective processes (collectively described as “non-orographic” generation). Of the two types, non-orographic generation is more poorly characterised, and is thus an area of significant current interest for weather and climate modelling research (e.g. Alexander *et al.*, 2010; Eckermann, 2011; Lott *et al.*, 2012; Kim *et al.*, 2013; Plougonven and Zhang, 2014; de la Cámara *et al.*, 2014; Bushell *et al.*, 2015).

One potentially significant non-orographic source of GWs is convection associated with tropical cyclones (TCs). These rapidly rotating storm systems are known by a variety of names including hurricanes and typhoons. They form over large bodies of warm water and cover regions hundreds of kilometres in diameter. The convective activity associated with them can, in the case of the largest TCs, extend as high as the tropopause.

Many previous case studies exist investigating GWs associated with individual TCs, using measurement methods as diverse as aircraft (e.g. Pfister *et al.*, 1993), balloon-based (e.g. Jewtoukoff *et al.*, 2013; Chane Ming *et al.*, 2014) and ground-based instruments (e.g. Sato, 1993; Tsuda *et al.*, 1994; Dhaka, 2003; Hecht *et al.*, 2009; Das *et al.*, 2012; Niranjan Kumar *et al.*, 2014), and satellites (e.g. Wu and Zhang, 2004; Hecht *et al.*, 2009; Kim *et al.*, 2009; Chane Ming *et al.*, 2014; Yue *et al.*, 2014). A wide range of modelling studies have also been carried out (e.g. Kuester *et al.*, 2008; Kim *et al.*, 2009; Chen *et al.*, 2012; Tang *et al.*, 2012; Kim *et al.*, 2014). The spectral range of stratospheric GWs observed or modelled in association with TCs is extremely broad and spans multiple orders of magnitude both in terms of vertical wavelengths (from as short as 0.7 km (e.g. Chane Ming *et al.*, 2014) to as long as 10 km or more [e.g. Wu and Zhang, 2004; Hecht *et al.*, 2009; Jewtoukoff *et al.*, 2013; Yue *et al.*, 2014]) and horizontal wavelengths (from tens of km [e.g. Dhaka, 2003; Das *et al.*, 2012] to thousands of km [e.g. Chane Ming *et al.*, 2010; Niranjan Kumar *et al.*, 2011; Chen *et al.*, 2012]), with a concomitantly broad range of wave amplitudes, propagation speeds and associated momentum fluxes.

However, such case studies inherently lack the geographic and temporal coverage needed to statistically characterise the global distribution of these TC-associated GWs. Addressing this issue, Hoffmann *et al.* (2018) used long-term estimates of variance in the stratospheric 4.3  $\mu\text{m}$  radiance channel of the Atmospheric Infrared Sounder (AIRS) instrument on NASA’s *Aqua* satellite to statistically investigate GWs generated by TCs over a 13-year period, using the International Best Track Archive for Climate Stewardship (IBTrACS) TC climatology (see section 2.1) to identify TC times and locations. They observed enhanced GW activity, in particular during the intensification phase of TCs. However, due to the nature of the AIRS instrument, their study was restricted to waves with very long vertical wavelengths ( $>\sim 10$  km)

and short horizontal wavelengths ( $<\sim 900$  km), which, due to their large horizontal-to-vertical wave number aspect ratio,  $k_h/k_z$ , must rapidly ascend vertically and require strong stratospheric background winds to be visible to AIRS. The strong background wind requirement also caused their results to exhibit a bias towards Southern Hemisphere TCs, which are fewer in number in the IBTrACS climatology than Northern Hemisphere TCs but are more often overlaid with regions of high wind speed due to the underlying atmospheric dynamics of the Southern Hemisphere. As such, they identified that waves in the Northern Hemisphere were likely to be more important than their study was able to measure, and that waves with shorter vertical wavelengths than observable by AIRS may be significant.

Here, I use data from the High Resolution Dynamics Limb Sounder (HIRDLS), Microwave Limb Sounder (MLS) and Sounding of the Atmosphere using Broadband Emission Radiometry (SABER) satellite limb sounders to address these issues. These instruments have observational filters (i.e. the spectral ranges of GWs that an instrument is capable of observing) suited to detecting GWs with vertical wavelengths  $>2$  km and horizontal wavelengths  $>200$  km, in strong contrast to the observational filter of AIRS (see fig. 9 of Wright *et al.* (2016) for further details on the observational filters of all four instruments; the stated values are for HIRDLS and are the best case). Combined, these three limb sounders provide hundreds of thousands of individual TC-associated GW measurements over more than a decade, which enabled me to quantify and statistically characterise the contribution of TC-associated GWs relative to other GW sources in the precise spectral regions Hoffmann *et al.* (2018) were unable to measure. In particular, the much reduced aspect ratio  $k_h/k_z$  of the GWs measurable by these instruments allows the study of GWs which ascend more slowly and at much shallower angles relative to those observed by AIRS, and strong background winds are not required to observe waves, which allows more detailed characterisation of Northern Hemisphere TCs.

To carry out this characterisation, I use TC data from the IBTrACS best-track database and GW observations from the specified limb-sounding instruments. I first assess a case study of a single large TC, Typhoon *Nabi* (2005), to demonstrate that TC-associated GWs can be observed and that, provided sufficient data are available, these observations are robust at the individual TC level. I then introduce a novel composite TC analysis of data from all available TCs during the periods of these satellite missions. This allows me to investigate statistically the effects of TCs in the general case, including assessments of their importance as a function of time, distance, magnitude and altitude. Finally, I extrapolate my results across the full IBTrACS dataset to assess and contextualise the combined contribution of TCs to the global GW momentum budget.

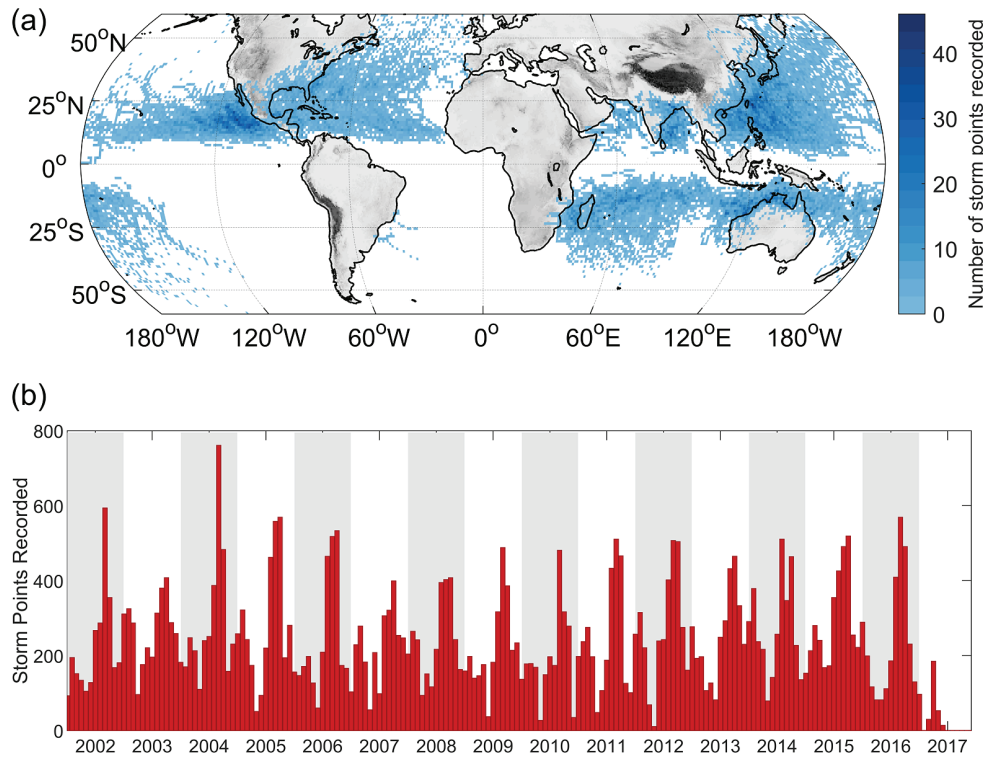


**FIGURE 1** (a) Map showing the geographic locations of all tropical cyclones (TCs) recorded in IBTrACS over the period 2002–2017. The scale bar indicates the raw number of individual recorded TC points within the grid cell rather than the number of distinct TCs. (b) Monthly total number of recorded TC points over the same time period

## 2 | DATA

### 2.1 | IBTrACS

I derive TC locations and properties from the International Best Track Archive for Climate Stewardship (IBTrACS) (Knapp *et al.*, 2010). IBTrACS is a composite dataset of track estimates for TCs, which combines data from multiple agencies to facilitate analysis. I specifically use data from version v03r10; these data have global coverage and cover the period from 1842 to 2017, with reduced coverage in the final year.

Figure 1a shows the geographic distribution of these observations over the time period 2002–2017, selected as a subset of the overall IBTrACS dataset for which GW data are available (see section 2.2), and Figure 1b shows the number of distinct observations per month over this period. Data have been interpolated to a 6-hr regular time-scale and wind speeds below 18 m/s have been removed (see below). Between 2002 and 2017, 45,421 observations were made of 1,379 TCs. The durations of individual TCs are approximately log-normally distributed, with a mean of 6 days and a standard deviation of 2 days. The shortest lasted 9 hr and the longest 26.75 days. Most major tropical and subtropical ocean regions are represented, with the exception that very few TCs are seen in the South Atlantic and Southeast Pacific basin. This is due to the underlying dynamics of TC formation rather than any deficiencies in the dataset.

Observations within each TC time series are not necessarily uniform in time: the smallest inter-observation time step for any given TC is 1 min and the longest is 1.75 days. However, the great majority of time steps between adjacent observations are either 6 hr (83%) or 3 hr (15%). To remove any bias in my final results due to this uneven sampling, I linearly interpolate all variables associated with each TC to a 6-hr scale and use the interpolated data for analysis.

For most analyses, I use the World Meteorological Organization's standardised portion of the overall IBTrACS product. This is a quality-controlled subset of the full dataset, which provides only limited information on TC properties beyond basic metadata such as their centre location and maximum sustained wind speed. In section 7, in order to better interpret my results, I also use additional estimates from a subset of data centres of TC radii of maximum wind (RMWs) and radii of outermost closed isobars (ROCI). These data are only available for ~50% of observations, primarily on the basis of the recording weather centre rather than magnitude or lifetime.

Finally, I omit TC observations with wind speeds below 18 m/s from my analyses. This cut-off is based on the Saffir–Simpson Hurricane Wind Scale definition of a tropical storm (section 8). I also omit observations poleward of 50°, since these are few in number and may differ statistically and dynamically from more typical TCs.

## 2.2 | GW observations

I derive GW properties from satellite observations of atmospheric temperature. Specifically, I analyse data from the High Resolution Dynamics Limb Sounder (HIRDLS) and Microwave Limb Sounder (MLS) on NASA's *Aura* satellite, and from the Sounding of the Atmosphere using Broadband Emission Radiometry (SABER) instrument on NASA's *TIMED* satellite. I use v7 HIRDLS data, v4.2 MLS data and v2.0 SABER data. Detailed information on the comparative GW detection characteristics of these datasets is provided by Wright *et al.* (2011) and Wright *et al.* (2016), and information on the more general properties of the three instruments and their retrievals is provided by Gille *et al.* (2013), Livesey *et al.* (2015) and Remsberg *et al.* (2008) for HIRDLS, MLS and SABER, respectively.

HIRDLS data cover the period from January 2005 to December 2007, MLS from August 2004 onwards, and SABER from January 2002 onwards. MLS data have near-global coverage, with profiles extending from 80°N to 80°S in latitude. HIRDLS has a similar northern limit, but a southern limit of 62°S. SABER coverage extends from either 80°N to 50°S or 50°N to 80°S in a yaw cycle with alternating 60-day phases. All three datasets thus cover the entire latitude range of my analysis throughout the year. Useful measurements extend from the tropopause to mesospheric altitudes for all three instruments.

To measure GWs present in these data and characterise their properties, I use the method of Wright and Gille (2013), which is based on the earlier work of Alexander *et al.* (2008). Briefly, in daily 5° latitude bins at each height level, the zonal mean temperature and the temperature amplitudes of the first seven planetary wave modes are computed, interpolated to the location of the individual measurement profiles and then removed to leave temperature perturbation profiles. These profiles are then Stockwell transformed (Stockwell *et al.*, 1996) and the complex transform output fields are multiplied together in conjugate pairs to produce covarying temperature estimates as a function of height and vertical wave number. At each height level, a single dominant peak is then extracted and compared to a noise floor computed from 10,000 randomly sampled profile pairs in the vicinity. If the peak is above the noise floor, then it is recorded as a wave and its horizontal wave number computed from the phase difference between the two members of each profile pair and their spatial separation (Ern *et al.*, 2004). Profile pairs more than 300 km apart are unlikely to contain signatures of the same wave, and are thus discarded before analysis (Ern *et al.*, 2011). I use data from altitudes of 18–80 km for my spectral analyses, with 20 levels of zero padding added above the top and below the bottom of this range to avoid spectral wraparound effects.

For each profile pair for which the separation distance and above-noise criteria are met, I estimate the covarying

temperature amplitude  $T'$ , the vertical wave number  $k_z$ , the horizontal wave number  $k_h$  and the momentum flux  $MF$ .  $MF$  is calculated as (Ern *et al.*, 2004)

$$MF = \frac{\rho}{2} \frac{k_h}{k_z} \left( \frac{g}{N} \right)^2 \left( \frac{T'}{T} \right)^2, \quad (1)$$

where  $\rho$  is atmospheric density,  $g$  is acceleration due to gravity,  $N$  is the buoyancy frequency and  $T$  is the background temperature. Wave numbers throughout this study are specified as  $1/\lambda$ , that is, without a factor of  $2\pi$  relative to wavelength. Since the measurements are of the covariation of GW properties within profile pairs, I geolocate the measurements at the mean location of the profile pair.

Table 1 of Wright *et al.* (2015) summarises the key limitations of this analysis technique. Three of these limitations are particularly important to properly contextualise the results presented here. These are (a) that measured  $T'$  values may be large underestimates of the true value, particularly at small vertical wave numbers where the Stockwell transform can suppress measured amplitudes by up to 25% even if fully resolved (Wright, 2010), (b) that measured  $k_h$  is the projection of the true value along the measurement track of the satellite, and thus will be an overestimate, perhaps significantly so (Ern *et al.*, 2004), and (c) that  $MF$  will also be strongly low-biased due to the combined effect of these two factors.

To assess any effect of the diurnal cycle on my results, all analyses were also repeated separately for the ascending-orbital node (i.e. northward-travelling) and the descending-orbital node (i.e. southward-travelling) subsets of the data. For HIRDLS and MLS, which have sun-synchronous orbits with an early-afternoon Equator crossing time in their ascending node, these subsets correspond to daytime and night-time data, respectively. The results did not change significantly, except for an increase in measurement uncertainty consistent with the reduction in data volume.

## 3 | METHODS

### 3.1 | Data selection

My goal is to assess the characteristics of TC-associated GWs. To achieve this, I first spatially and temporally subcategorise the satellite GW observations according to the geographic and temporal regions of anticipated effect. I define this as all GW observations within 1,000 km of each TC centre, and within ±15 days of the TC centre's time at that location. This time window is intentionally wide, and is reduced in later sections of the study based on preliminary results to just the period of heightened GW activity revealed by the wider analysis.

The distance range is defined on the basis of linear GW theory (e.g. Fritts and Alexander, 2003). This suggests that, for waves in the observational filter of the instruments

under consideration, typical horizontal group velocities should be  $\sim 5\text{--}30 \text{ m/s}$  and vertical group velocities should be  $\sim 0.05\text{--}0.5 \text{ m/s}$ . A wave with such a vertical group velocity will ascend from the mid-troposphere to my main analysis height level of 36 km in altitude (see section 3.2) in around 1–10 hr. In the same amount of time, it will propagate a horizontal distance of 300–800 km, and thus, assuming the TCs generate waves in the instrument observational filter, waves should primarily be observed within approximately this radius of the TC. Assuming that most waves are generated in the core region of the TC, and allowing for TC radii of maximum winds  $\sim 100\text{--}200 \text{ km}$  (section 7), this implies that a cut-off distance of 1,000 km should identify a large fraction of the waves generated by the TCs. However, in practice I observe heightened GW effects at much larger horizontal distances from the TC centre than this; this is discussed further in section 7.

The time range is more arbitrarily defined. Since the temporal resolution of the majority of the IBTrACS dataset is 6 hr, and TC centres typically move by much less than 1,000 km in this time, the dominant temporal selection effect for my analysis is best defined in terms of the travel speed of the TC rather than the waves it generates. As discussed in section 2.1, the mean temporal duration of TCs in the IBTrACS dataset is  $6\pm 2$  days, and thus a time window of 15 days before and after the TC centre should be sufficient to include the vast majority of TC-generated waves and also an element of background to which these measurements can be compared. Sections 4 and 5 use this broad  $\pm 15$ -day window, while sections 7 onward use a narrower window of  $-2$  to 0 days before the TC, chosen on the basis of the results presented in section 5. In these sections, the period from  $\pm 13$  to  $\pm 15$  days is used as a background for comparison.

### 3.2 | Altitude of observations

GW observations from limb sounders can be strongly affected by temperature signals from sources other than the waves themselves. This can affect measured GW effects at relatively large vertical displacements from the nominal measurement altitude, due to the inclusion of a range of altitudes in the spectral analysis windows used.

For this study, the two most important such signatures are high-altitude cloud and the sharp reversal in gradient of atmospheric profiles at the tropopause. The latter in particular can dominate GW analyses of this type, particularly in the tropics and inner subtropics where the tropopause may reach  $\sim 18 \text{ km}$ .

In my analysis, I allow GWs to be recorded with vertical wavelengths as long as 18 km; thus GWs detected at a given height may potentially incorporate signals from as far away as this. However, in practice most detected GWs have much shorter wavelengths (see, e.g., Figure 8), and due to the spatial localisation inherent in the Stockwell transform analysis the

dominant portion of the signal will tend to be centred near the altitude of interest.

Nevertheless, to prevent this effect from influencing my results, I perform my analyses at 36 km altitude, that is, the upper bound of vertical wavelength above the upper bound of possible tropopause height. Lower altitudes could give useful data, but come with the risks of abnormally high cloud-top heights associated with particularly large TCs skewing the results and of vertically long waves being edge-truncated.

### 3.3 | Data analysis

For each TC centre at each time point in the 6-hr interpolated IBTrACS dataset, I measure and record all GW measurements within 1,000 km and 15 days, together with their time difference, distance and direction relative to the TC centre.

This process is illustrated by Figure 2a. Here, the TC centre is indicated by the solid brown circle at the centre of the diagram, and the 1,000 km distance limit is indicated by the concentric dashed circle. Nine example satellite GW measurements are then indicated by solid shapes labelled  $M$ , with subscripts indicating their measurement times in days relative to the TC centre measurement. The points indicated by red squares are excluded on the basis of time – they lie more than 15 days before or after the TC centre measurement. The points indicated by black triangles are valid in terms of time, but excluded for reasons of distance – they lie more than 1,000 km away from the TC centre. The points indicated by blue circles are valid – they lie within 1,000 km of the TC centre at time lags of less than 15 days.

For each of these points I then retain their distance  $r$ , bearing from the north relative to the TC centre  $\theta$  and the time difference from the TC centre, shown as an example for the blue circle near the top right. This process thus provides, for each TC observation, a list of all GW observations that are spatially close to the TC centre, at a range of time lags from  $-15$  to  $+15$  days, together with their spatial relationship to the TC centre at that time.

If the TC centre is moving sufficiently slowly that it remains within 1,000 km of a GW observation, which is usually the case, a single observation could in principle contribute to comparisons at multiple lags. To avoid this, I next identify all the duplicate copies of the same observation in the final data product and select only the copy with the smallest time difference from any TC centre.

Figure 2b illustrates this process. The orange line shows the path of a TC, which was centred on the four consecutive orange and brown points along the line at time points  $t_1\text{--}t_4$ . The 1,000 km spatial window around the TC centre for each time is indicated by the correspondingly coloured dashed circles. Three GW measurements,  $M_1$ ,  $M_2$  and  $M_3$ , taken during the passage of this TC are then indicated by blue dots, at times  $t_1$ ,  $t_2$  and  $t_3$ , respectively. Measurement  $M_1$  (the rightmost)

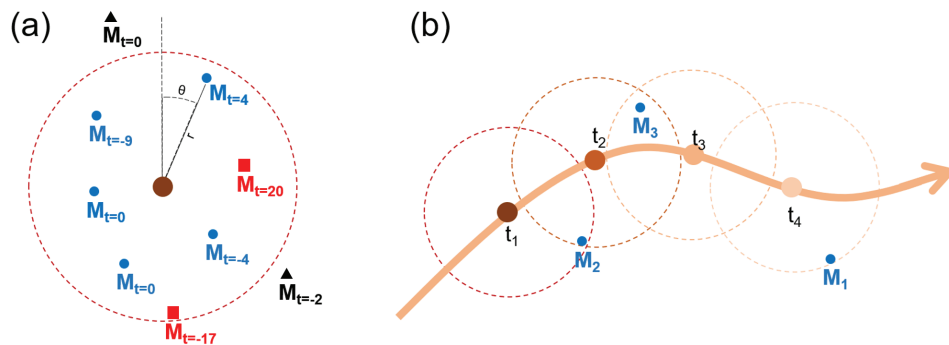


**FIGURE 2** Diagram illustrating (a) which gravity wave (GW) observations are retained for each TC centre and (b) how GW measurements could contribute to estimates of the TC effects at multiple lags if duplicates were not removed. See the text for details

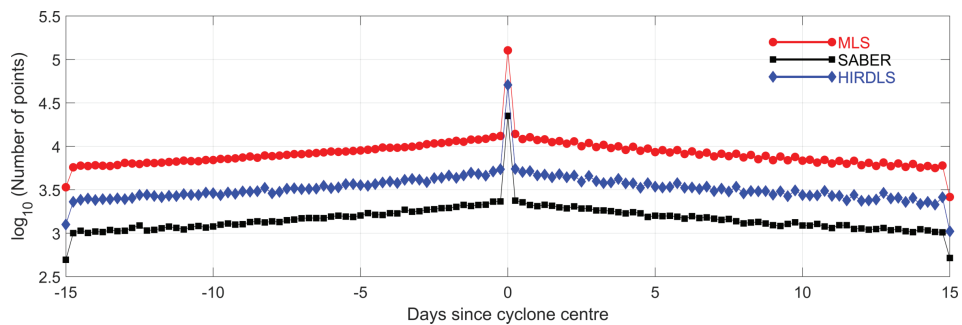


**FIGURE 3** Number of measurements over all TCs from each instrument per quarter-day period in the time window. Note the very large peak at zero lag and the steady symmetric drop away from this point in both directions, both of which are features that arise from the deduplication process

will contribute to the TC effect estimate at time  $t_4$  with a lag of +18 hr (i.e. three time points), as it only lies within the averaging radius at time  $t_4$ ; at no other time does it lie within the 1,000 km radius of any other TC centre. By the same logic, measurement  $M_2$  (the leftmost) should contribute to the TC estimates at  $t_1$  with a lag of -6 hr and to the estimates at  $t_2$  with a lag of 0 hr, but I remove the -6-hr lagged copy and retain only the 0-hr lagged copy. Similarly, measurement  $M_3$  should contribute to the estimates at  $t_2$  with a lag of +6 hr and at  $t_3$  with a lag of 0 hr, but the +6-hr lagged copy is discarded.

This deduplication process produces a bias in the number of samples per timestep towards smaller time differences. This is illustrated by Figure 3, which shows the number of measurements per 6-hr lag bin for each instrument over the time range considered. For all three instruments, there is a very large peak in the number of GW measurements at a lag of 0 days, with an immediate sharp drop followed by a steady near-symmetrical decline on both sides of the peak. This is intuitively sensible, since preference in the deduplication process is always given to a lag closer to zero. This should not affect the magnitude of the results presented, which use medians and distribution statistics, but will affect the range of uncertainties associated with each time point (see section 3.4).

To assess the effects of this, the analyses were performed separately with duplication permitted and the same form of results was seen, but with much smaller magnitudes for the change in variables. This is consistent with the expected effect

of including measurements at high time lags which would have been closer to the TC centre at shorter lags, and would thus skew the resulting averages high.

### 3.4 | Parametric versus non-parametric methods

GW properties typically have non-Gaussian distributions, most commonly the log-normal distribution (e.g. Nastrom and Gage, 1985; Hertzog *et al.*, 2012; Wright *et al.*, 2013; Wright *et al.*, 2017). To avoid any issues resulting from this, I use non-parametric statistics.

Uncertainty bounds are computed using the statistical bootstrap (Efron, 1979), with the 2.5th, 16th, 84th and 97.5th percentiles computed and stored. These correspond to the distance of the first (16–84%) and second (2.5–97.5%) standard deviations from the mean for a Gaussian distribution, and are thus equivalent to the standard error on the statistical property under consideration at 68% and 95% confidence, respectively (Guan, 2003). For brevity I refer to them throughout as the  $\text{SE}_{68}$  and  $\text{SE}_{95}$  bounds. I also compute the median of the bootstrap definition, which is used as my primary characterisation statistic, since means will skew high for log-normal data. All bootstrap analyses use 1,000 resamplings of the same number of elements as the original series. Note clearly therefore that plotted uncertainty bounds represent my certainty in the estimated statistic, *not* the distribution of measured values.

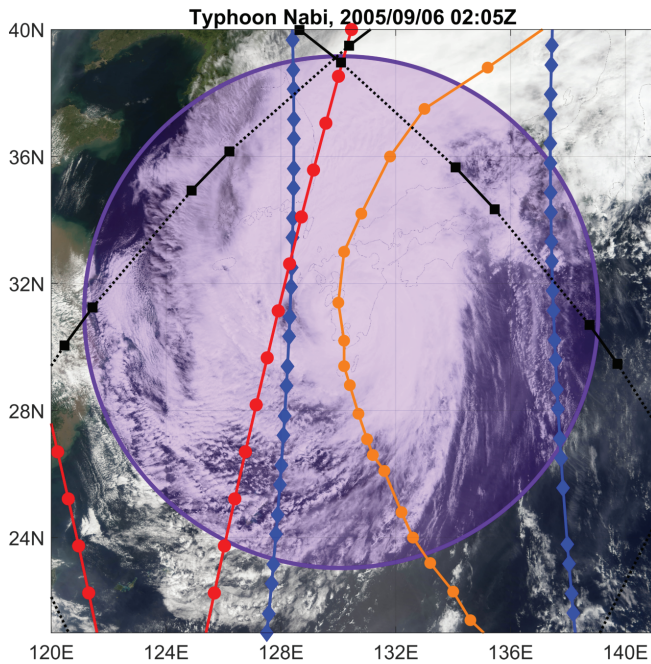


**FIGURE 4** Background: Image of Typhoon *Nabi*, from NASA/MODIS data processed by Jesse Allen of the NASA Earth Observatory. Orange line/circles: Path of the typhoon over the region, with circles indicating distance travelled per quarter day from south to north. Purple circle: 1,000 km radius centred on the TC at this time, indicating the region the analysis would flag as being above the TC centre. Red, blue and black lines: Limb sounder overpasses on the same day, with profile-centre locations indicated by coloured circles

An exception to this are the results presented in section 8, which use the mean as their primary statistic. This is to facilitate comparison with other studies and to allow estimation of basin-total TC-associated GW effects at the annual scale.

## 4 | CASE STUDY: TYPHOON *NABI*, 2005

I first illustrate my method using the case study of Typhoon *Nabi*. This super typhoon, which struck the coast of Japan in September 2005, was the equivalent of a Category 5 hurricane on the Saffir–Simpson Hurricane Wind Scale (see section 6.1), with peak sustained winds reaching speeds of  $>70$  m/s.

### 4.1 | Data footprints relative to MODIS imagery

Figure 4 shows a NASA/MODIS image of *Nabi* at 0205 UTC on September 6, 2005, around two thirds of the way through its life cycle. At the time of the closest IBTrACS observation to the image (0300 UTC on the same day), the TC centre was estimated at  $32^\circ\text{N}$ ,  $130^\circ\text{E}$ , with a wind speed of 40 m/s. The orange line indicates the approximate track of the typhoon over the time period immediately before and after

this, with sequential orange circles indicating 6-hr time steps from southeast to northeast.

Overlaid on top of this, I show the measurement tracks from HIRDLS (blue diamonds), MLS (red circles) and SABER (black squares) on the same day. The markers indicate the centre of the measurement volume for each profile, with temporally adjacent profiles connected by lines. Solid lines indicate profile pairs used in my GW analysis, while dotted lines (SABER only) indicate pairs that are too widely separated to provide GW data. Note again that I geolocate my measurements at the mean pair location, that is, halfway along the solid lines joining each pair of circles. Finally, the purple shaded circle shows the 1,000 km region I consider as co-located with the TC for the analysis.

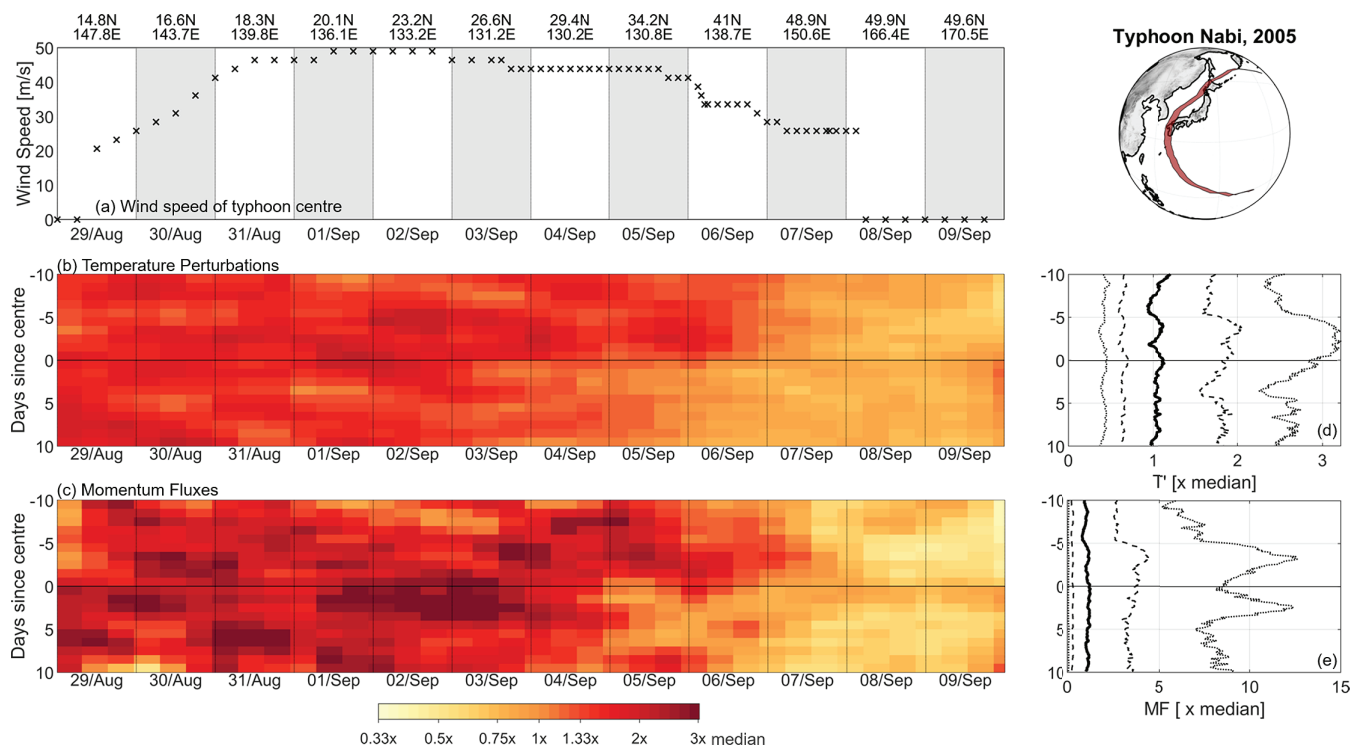
### 4.2 | GW effects of Typhoon *Nabi*

Figure 5 examines the GW's observed temperature amplitude  $T'$  and momentum flux  $MF$  associated with Typhoon *Nabi*. To contextualise the results, Figure 5a shows a time series of IBTrACS-recorded wind speed, together with a map of the TC path, which travelled clockwise along the track shown. The latitude and longitude of the TC centre at 1200 UTC on each day is indicated above the wind time series.

Figures 5b and 5c show the observed GW  $T'$  and  $MF$ , respectively. The horizontal axis shows measurement times and the vertical axis shows the number of days since the TC passed the location. Colours then show the median values of the properties in bins of one third of a day horizontally and 1 day vertically, with duplicate profiles removed as described above. For this section only, data from all three satellite instruments have been combined and normalised by their median value over the period in order to facilitate full temporal coverage. This median is defined over all GWs recorded within 1,000 km and  $\pm 15$  days of Typhoon *Nabi* at any point in its life cycle. Data have been boxcar-smoothed by three bins both horizontally and vertically to aid interpretation.

The dominant variability is a function of the date, with large values of both  $T'$  and  $MF$  observed during the early high-wind-speed period of the typhoon and smaller values observed as it dies away. Some of the later drop may be due to the underlying geographic distribution of GWs, as there is less GW activity at the higher latitudes through which the typhoon passes late in its life cycle; however the difference across this geographic range in other years is significantly smaller than the effect seen here. Aside from this, it is difficult to see the effect of time lag on either  $T'$  or  $MF$  due to the considerable internal variability of each dataset even after smoothing.

To show the lag effects more clearly, Figures 5d and 5e show the distribution of  $T'$  and  $MF$  against lag averaged over all dates. For each panel, the thick black line shows the median value, the dashed lines the 16th and 84th percentiles, and the dotted lines the 2.5th and 97.5th percentiles. In both cases, very little variability is observed in the 2.5th, 16th



**FIGURE 5** Analysis of the observed GW  $T'$  and  $MF$  from Typhoon *Nabi*. (a) Time series of wind speeds at the TC centre. (b,c) Median  $T'$  and  $MF$  within 1,000 km of the TC centre against time (horizontal axis) and lag (vertical axis). (d,e) Time-mean  $T'$  and  $MF$  as a function of time lag from the TC centre. Thick black lines indicate the median, dashed lines the 18th and 84th percentiles, and dotted lines the 2.5th and 97.5th percentiles

and 50th percentiles, but more variability is seen at the 84th and (particularly) the 97.5th percentiles. This is consistent with a non-unity probability of wave observation for any given measurement due to wave intermittency effects, which can be considerable for non-orographic wave sources such as these (e.g. Wright *et al.*, 2013). At the 97.5th percentile, one observes a peak in  $T'$  of  $\sim 3 \times$  the median value over the period a few days before the TC centre, and two peaks in  $MF$  with values of  $\sim 13 \times$  the period median, one a few days before and one a few days after the TC.

## 5 | COMPOSITE CYCLONE TIME-SERIES ANALYSES

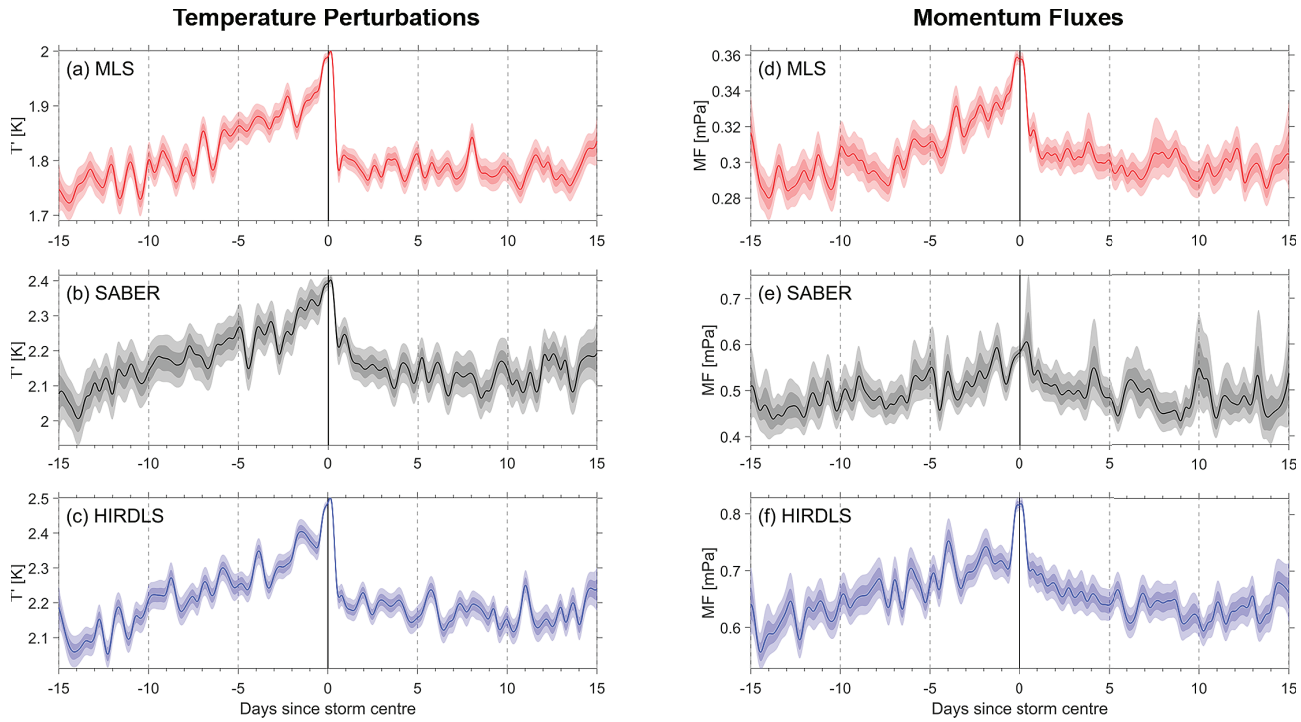
The large number of GW measurements spatially and temporally co-located with Typhoon *Nabi* is atypical for these datasets. Consequently, a direct analysis such as this cannot be used to study individual TCs in the general case. Accordingly, to further study and characterise TC-related GWs, for the remainder of this study I use a composite analysis which combines GW measurements from all available TC tracks in the IBTrACS dataset. This allows statistical conclusions to be drawn from the sparse data.

Figure 6 shows composite time series for GW  $T'$  and  $MF$ , combining all IBTrACS-recorded TCs between 2002 and 2017. To produce these, I average the observed GW variables for all limb sounder profiles within 1,000 km of all

TCs at all time steps; that is to say, I treat each TC *observation* rather than each *complete TC* as an individual point. Each panel then shows data as a function of the (positive or negative) lag between the satellite observation and the TC observations.

Figure 6a–c shows  $T'$  and Figure 6d,e,f shows  $MF$ . The coloured time series show the median for each time step, in half-day bins, stepping each bin by a quarter of a day. Coloured regions around the line series show confidence intervals on this median, with lighter shades indicating the  $SE_{95}$  of the median and darker shades  $SE_{66}$ . Note that, unlike for the example of Typhoon *Nabi*, TC-associated GW effects are now clearly visible in the median estimate, consistent with the increased certainty permitted by larger-number statistics.

For all three instruments and for both  $T'$  and  $MF$ , a consistent pattern is seen. Observed GW activity steadily builds up over the 10 days before the TC, reaching a peak at zero lag, that is, the time of the TC itself. This is followed by a sharp discontinuity, with GW activity dropping rapidly to a much lower level. Observed  $T'$  values drop to a level lower than the entire week before the TC and remain stable at a level similar to that recorded around a fortnight before the TC. For  $MF$ , the drop is gentler, falling quickly to the level reached around 1 day before the TC centre but then declining relatively smoothly to reach background levels around a week after the TC. For  $T'$ , the peak value reached is  $\sim 15\%$  above the background levels seen a fortnight before and after the TC, while for  $MF$  the peak is  $\sim 20\text{--}30\%$  above background levels.



**FIGURE 6** Time series of (a,b,c)  $T'$  and (d,e,f)  $MF$ , compositing over all TCs. Coloured time series show the measured property, with progressively darker shading indicating the 5–95th and 16–84th percentiles of the bootstrap-derived distribution of the possible medians of the data

Absolute magnitudes of both  $T'$  and  $MF$  are largest for HIRDLS and smallest for MLS. This is consistent with the relative vertical resolution of the three instruments. At this altitude level, HIRDLS has a relatively high vertical resolution of 1 km and can thus resolve the maximal amplitudes of relatively large- $k_z$  GWs, while SABER and MLS have coarser vertical resolutions of 2 km and 5 km, respectively, and will thus underestimate wave amplitudes. The combination of these two effects will lead to overall smaller magnitudes in  $T'$  and derived properties (i.e.  $MF$ ) and an inability to measure the shortest vertical wavelength waves seen in the HIRDLS data. This effect is also seen strongly in Figure 8.

It is important to note that the discontinuity at the TC centre is asymmetric, with a steady build-up followed by a rapid decline. This matters because the number of contributing measurements is also strongly discontinuous at this point (Figure 3), but the discontinuity in number is symmetric about zero lag. In order to further confirm that the discontinuity does not arise as a result of the number of measurements, the analysis was repeated with a constant number of points bootstrap-sampled at each time point instead of the full number of available points. Both  $10^3$  and  $10^5$ , that is, the lower-bound and upper-bound number of points contributing at each time step, were used. The same discontinuity was seen in both cases, with the same magnitude relative to background.

Another possibility is that the sharp drop at zero lag may be due to an asymmetry in wave propagation direction away from the TCs. To test this, the spatial distributions of measured  $T'$

and  $MF$  relative to the TC centre were examined, subdivided by a range of possible controlling parameters including basin, point in TC life cycle and net propagation direction of the TC centre. Results (omitted for brevity) were highly inconsistent between events and between the three different datasets, suggesting that if this is a factor, then it is not dominant.

Figure 7 shows the results of an equivalent analysis carried out for  $k_h$  and  $k_z$ . Due to noisier data for these variables, this analysis is carried out in bins twice as large: 1-day bins stepping each bin by half a day. The results for this are less clear-cut. There is perhaps some evidence of a drop in  $k_h$  just before the TC centre, most clearly for HIRDLS and MLS where it contributes to the sharp peak seen in  $MF$ , but the change is fractionally small due to the major issues involved in measuring GW horizontal wavelength from limb-sounder profile pairs as discussed in section 2.2. There is also perhaps some evidence of a reduction in  $k_z$ , but this is even weaker than for  $k_h$ . This suggests that the changes seen in  $MF$  are primarily driven by changes in the measured ratio  $(T'/\bar{T})^2$  rather than wavelength.

From these results, I conclude that (a) a measurable and statistically significant additional GW signal is observed in the period immediately before the TC centre, dropping rapidly immediately after the TC passage; (b) enhanced GW activity is seen for up to two weeks before the TC passage; and (c) any effect on GW wavelength in either the horizontal or vertical is either weak or invisible to these instruments, with the possible exception of HIRDLS, being the instrument with the highest spatial resolution in both dimensions.

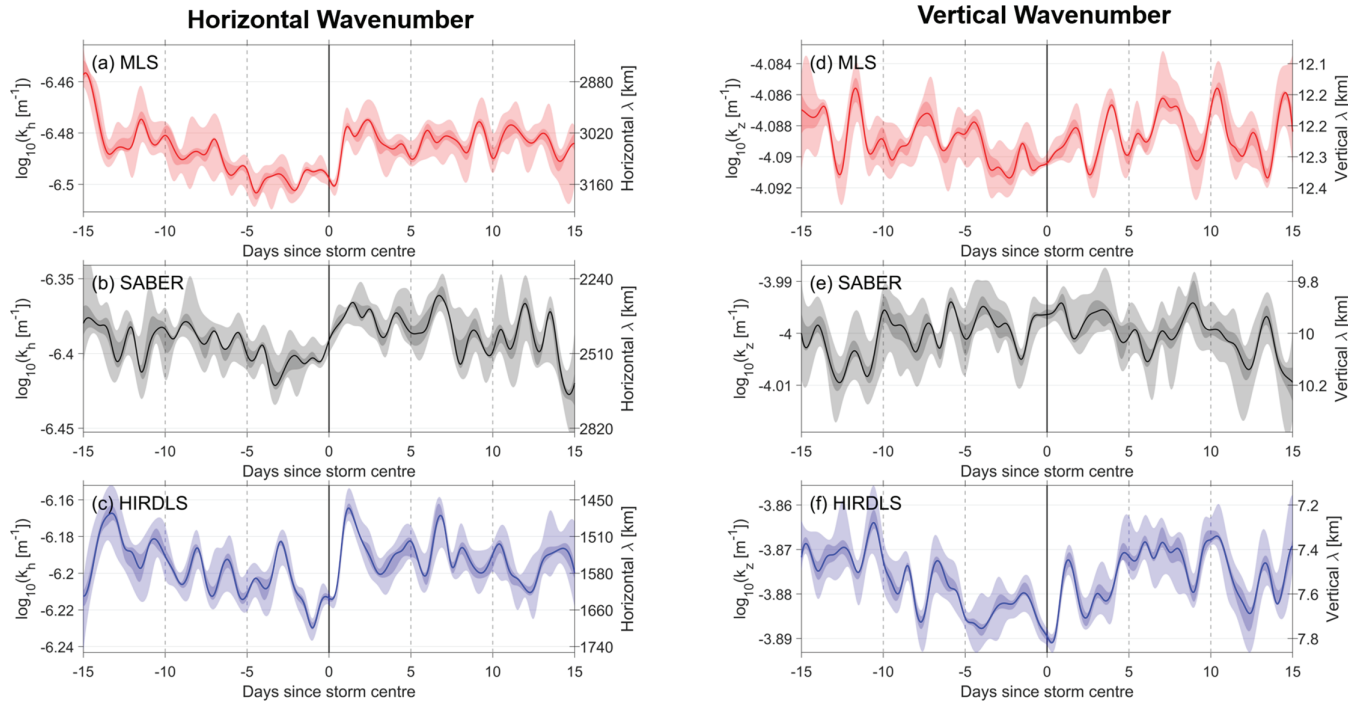


**FIGURE 7** Time series of (a,b,c)  $k_h$  and (d,e,f)  $k_z$ , composited over all TCs. Coloured time series show the measured property, with progressively darker shading indicating the 5–95th and 16–84th percentiles of the bootstrap-derived distribution of the possible medians of the data

## 6 | STATISTICAL ANALYSES

### 6.1 | GW effects by TC category

TCs, especially in the North Atlantic basin, are often classified using the Saffir–Simpson Hurricane Wind Scale (SSHWS). This scale subdivides observed TCs into seven classes according to maximum sustained wind speed, with TCs reaching wind speeds below 17 m/s classified as tropical depressions, between 18 and 32 m/s as tropical storms and above 32 m/s as hurricanes, subdivided into Categories 1–5, with lower cut-offs at 33, 43, 50, 58 and 70 m/s, respectively. Although significant criticisms of the scale exist, such as that it does not take account of otherwise important effects such as storm surge magnitude or precipitation volume, it does provide a simple way of broadly classifying observed TCs by magnitude.

Figure 8 categorises my GW observations according to the SSHWS. Specifically, for each TC observation, I use wind speed to categorise the TC and then compute the probability density distribution (PDD) of GW properties measured by profiles from  $-2$  to  $0$  days of all TC centres in each category.

I compute PDDs for tropical storms (“TS”) and Category 1–5 hurricanes, together with distributions for all TCs (“All”) and background (“BG”). The background estimate is produced from a random sample of profiles  $\pm 13\text{--}15$  days from the storm centre, with the same number of samples as in the equivalent “All” distribution.

Results are shown as violin plots, produced using kernel density methods. I use the Epanechnikov kernel with a bandwidth of five bins (except for  $k_z$ , which has 10 bins due to the Stockwell-transform vertical wave number estimates being restricted to integer divisors of window height by the underlying fast Fourier transform algorithms used). The same analyses were also performed with different bandwidths (1–50 bins) and kernels (normal and box kernels, with the same range of bandwidths) and the results remained robust. The violin plots are then overplotted with box plots of the summary statistics of the distribution. Specifically, the width of the shaded region (the “violin”) indicates the proportion of measurements and the overlaid box plots indicate the median (crosses), the 18th and 82nd percentiles (boxes), and the 2.5th and 97.5th percentiles (whiskers). The numbers in small print below each violin plot indicate the number of contributing GW measurements.

The observed PDDs for all three instruments are broadly similar in form but with constant offsets and scalings that are consistent with other results presented in this study. To avoid unnecessary duplication, in Figure 8 I show the data subdivided by TC category for MLS only, which has the largest number of useful profiles, and provide summary PDDs (“All” and “BG”) for SABER and HIRDLS.

I first consider  $T'$  (see Figure 8a). In the “all measurements” distributions (rightmost six violins), an increase in  $T'$  relative to background is seen for all three instruments, of broadly similar fractional size. The increase is in the form of a positive shift across the whole distribution, with fewer small

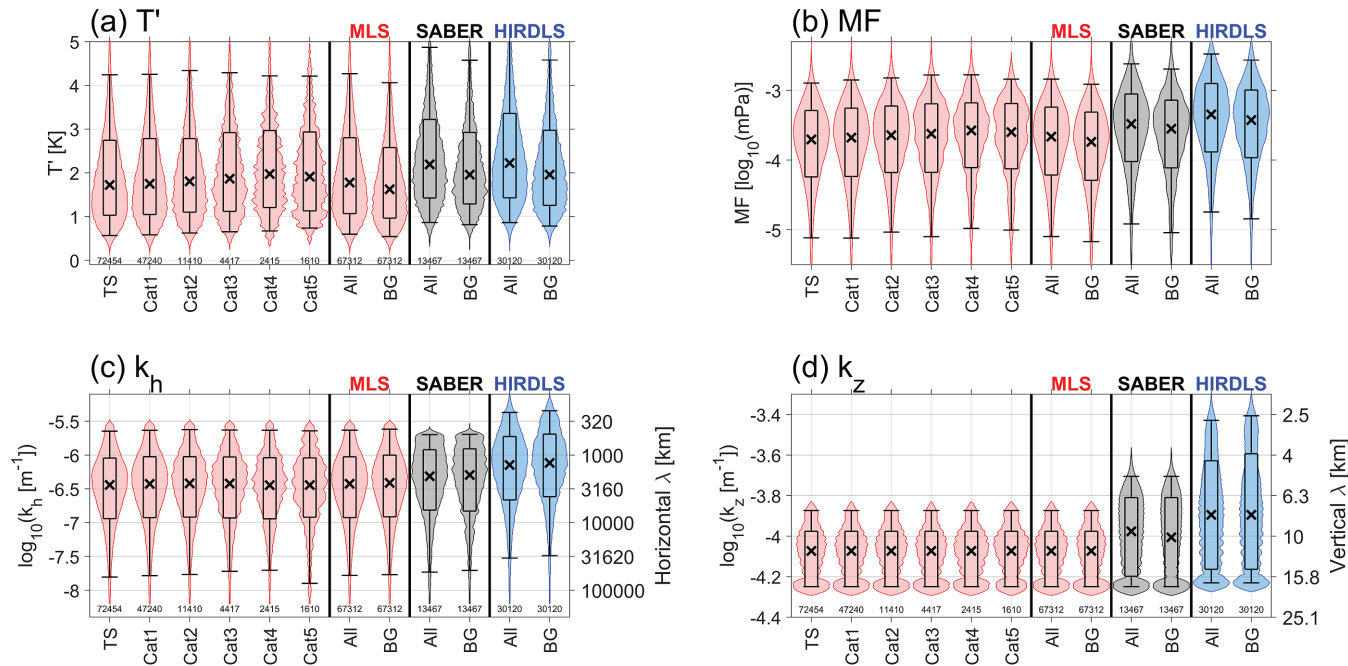


**FIGURE 8** Violin plots of the GW properties as described in the text, shown for all TC categories (“All”) and background (“BG”), for MLS (red), SABER (black) and HIRDLS (blue). For MLS, data have been subdivided according to SSHWS categories. Both SABER and HIRDLS show similar distributions but with scaled offsets, and have been omitted for clarity. Small numbers below each violin indicate the number of profiles contributing to the sample

values for the “All” distributions relative to background as well as more large values. Each distribution is unimodal and takes the form of a positive-skewed log-normal distribution, consistent with previous GW studies (e.g. Nastrom and Gage, 1985; Hertzog *et al.*, 2012; Wright *et al.*, 2013). Differences in  $T'$  between categories are small, with all medians within a 0.25 K range. Observed  $T'$  rises with category between TS and Category 4, with a small drop at Category 5. All distributions are again unimodal, positive-skewed and log-normal.

Results for  $MF$  (see Figure 8b) are very similar to those for  $T'$ , with increased  $MF$  over TCs relative to background, a steady increase with intensity up to Category 4 and then a drop for Category 5. Distributions are again unimodal, positive-skewed and log-normal (note that the vertical axis for this figure is logarithmic, and thus the distributions appear closer to Gaussian than for  $T'$  but have similar skew in linear space).

Results for  $k_h$  and  $k_z$  (Figures 8c and 8d) show less variability, consistent with section 5.  $k_h$  is very slightly smaller over TCs than over background, but this difference is very small in terms of both the summary statistics and the distribution as a whole. No significant differences are seen for  $k_z$ .

## 6.2 | Proto-hurricanes versus tropical storms

Figure 9(a) applies the same analysis as Figure 8, but with the data divided into TCs which do and do not later develop

into Category 3 or higher hurricanes later in their life cycle. As with section 6.1, data from the –2 to 0 days after the TC centre are used for this analysis.

Specifically, I first identify for each TC whether any point in the 6-hr-interpolated time series reaches Category 3 or higher, discarding all the time points after the first time that this occurs in each record. The remaining data are then divided into two sets: (a) those that do and (b) those that do not reach this intensity. The same statistical analyses as in section 6.1 are then performed.

The overall distributions are similar to those seen above. However, a measurable shift is seen towards larger  $T'$  values for TCs that will later develop into hurricanes than for those that do not. This difference is approximately 15% at the median level of the distribution (15% for MLS and HIRDLS; 10% for SABER) and around 5% at the 97.5th percentile. For brevity, only  $T'$  data are plotted; for reference, at the distribution median  $MF$  shows an increase of ~15%, while  $k_h$  and  $k_z$  both show a reduction of ~10%; that is, longer wavelengths are associated with developing hurricanes.

These results strongly suggest that more intense GW activity is associated with TCs that will later develop into hurricanes or typhoons. This in turn reinforces the hypothesis of Hoffmann *et al.* (2018) that stratospheric GW measurements can provide additional information that is useful for predicting intense hurricanes, the early development of which would otherwise be obscured from satellite measurements by tropospheric cloud.

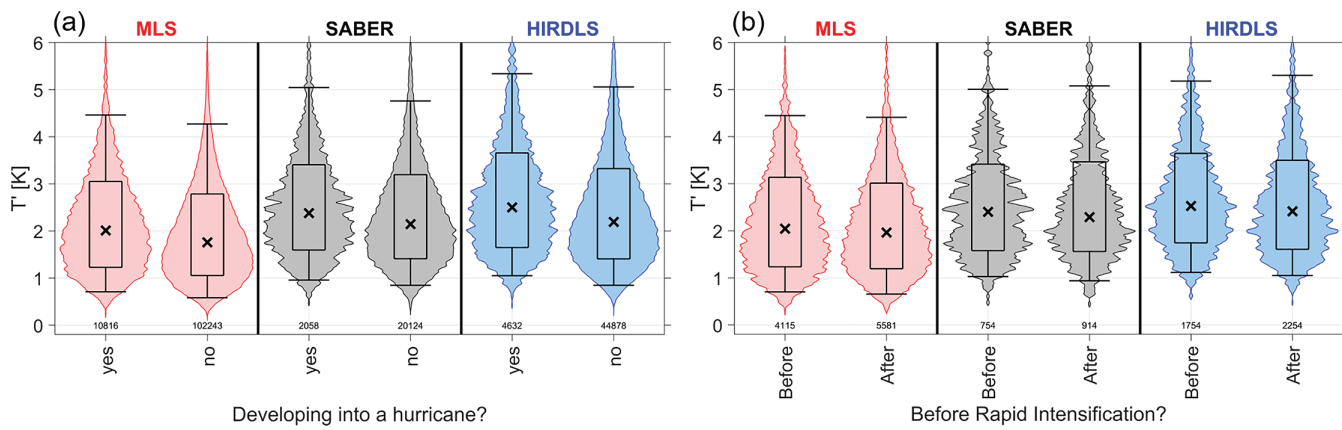


**FIGURE 9** Violin plots of measured  $T'$  to better characterise TCs that reach Category 3 during their life cycle. (a) Measured values for all TCs which (left) do and (right) do not reach Category 3 later in their life cycle. (b) Measured values from (left) 2 days before to 0.5 days before and (right) 0.5 days to 2 days after rapid intensification. Small numbers below each violin plot indicate the number of profiles contributing to the sample

### 6.3 | GW effects of rapid hurricane intensification

Figure 9(b) shows the data divided into time points (left) before and (right) after rapid intensification (RI). Since this comparison is focused on a primarily temporal effect, only GW measurements within  $\pm 0.25$  days (i.e. one IBTrACS time step) of the TC centre are used; this provides much fewer samples, leading to much noisier distributions.

I use the United States National Hurricane Center definition of RI. This defines a TC as having rapidly intensified if the associated wind speed increases by 15.4 m/s (30 knots) in a 24-hr period. To identify cases of RI, I find the first time point in each TC time series for which this definition is reached, discarding all time series in which it is not. For each remaining TC, I then extract the period from 0.5–2 days before (left) and after (right) the time at which the condition was met, with zero time shift defined as the midpoint of the 24-hr period of first RI. I then analyse the resulting GW data in the same way as above. Slightly more GW measurements contribute to the ‘‘before’’ distributions than to the ‘‘after’’ distributions; this is because many measured TCs exhibit RI very close to the start of their data records, and thus fewer profiles can be definitively associated with the pre-intensification phase.

Much smaller differences are seen than in the previous section. Distribution median  $T'$  values after RI are 5% lower for all three instruments than before RI. Changes at the 97.5th percentile are inconsistent between instruments; however, this is primarily due to the very small number of profiles contributing – for example, only 19 profiles lie above the 97.5th percentile of the SABER ‘‘before’’ distribution. Thus, while the results of this analysis suggest that the composite TC results presented in section 5 hold true at a statistical level for individual cyclones, there are insufficient data available to confirm this fully.

### 7 | DISTANCE FROM CYCLONE CENTRE

Figure 10 shows measured  $MF$  at increasing horizontal distances from the TC centre, both up to 4,500 km away from the TC (Figure 10a) and separately within just the 1,000 km measurement radius defined above (Figure 10b). As previously, lighter shading indicates  $SE_{95}$ , darker shading  $SE_{66}$  and the solid line the median. The horizontal axes show the distance from the TC centre and the vertical axes show the observed  $MF$ , scaled for each dataset to equal unity at 1,000 km. Data have been analysed in 100 km radial distance bands stepped 5 km apart and, based on the above analyses, I use data from 2 days before to 0 days before the TC centre in order to focus on the period of heightened  $T'$  and  $MF$  observed earlier.

To provide an indication of the areal extent of the TCs studied relative to their measured GW effects, the orange and green kernel density plots in the lower half of Figure 10 show ROCI and RMW estimates from the portion of IBTrACS for which these data are available. These plots have been normalised to equal one at their respective peaks.

At short distances from the TC centre, one observes significant variability in estimates of GW  $MF$ . This is primarily due to the decreasing number of profiles in annuli of fixed width but narrowing radius, and also leads to very wide  $SE_{66}$  and  $SE_{95}$  bounds at short distances. This is particularly the case for SABER, where the median GW  $MF$  estimate drops below the 1,000 km estimate at short distances but with extremely large uncertainty bounds. SABER’s larger uncertainties at short range are consistent with the limited horizontal resolution of the instrument relative to MLS and HIRDLS (e.g. section 4; for more detail see Wright and Hindley 2018), which makes highly precise spatial estimates challenging to perform accurately.

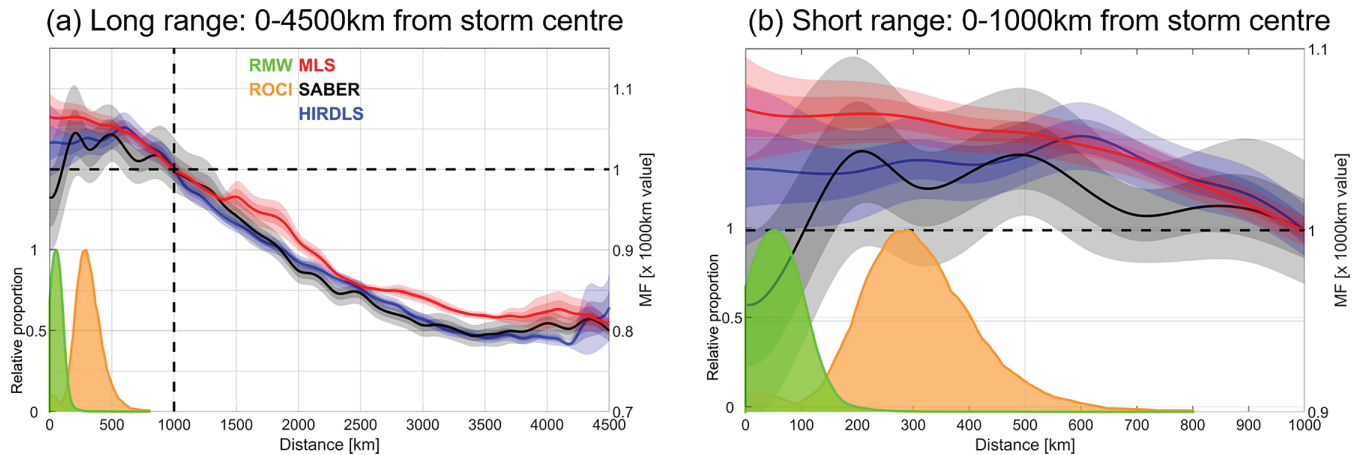


**FIGURE 10** Red, black and blue lines: Observed momentum flux as a function of distance from the TC, scaled to equal one at 1,000 km. Progressively darker shading indicates the SE<sub>95</sub>, SE<sub>66</sub> and mean of the data. Kernel density plots show (green) radius of minimum winds (RMW) and (orange) radius of outermost closed isobar (ROCI) for TCs for which these data are available. Panel (b) shows the region within 1,000 km of the TC centre, while panel (a) extends the range up to 4,500 km

At distances larger than  $\sim$ 600 km from the TC centre ( $\sim$ 800 km for SABER), the measured  $MF$  steadily and near-monotonically decreases with distance until it begins to stabilise at around 3,000–3,500 km from the TC centre (extended analyses, not shown, suggest that the plateau reached in this region continues to a distance of at least 8,000 km). This could either be due to the generation of waves by surrounding weather systems being temporally correlated with the TC systems, or to the propagation of extremely shallow inertia GWs away from the TC centre. The latter is more likely, since it is also consistent with the observational filter of these instruments, which will tend towards the measurement of longer horizontal wavelengths (e.g. Ern *et al.*, 2004; Wright *et al.*, 2015). There will also be some effect caused by the underlying geographic variability of other GW sources: TCs predominantly peak at latitudes  $\sim$ 10–30°, and distances of the order of thousands of kilometres will include regions such as the Poles and the Equator where previous studies with these instruments show lower “background” GW activity.

## 8 | CONTRIBUTION TO THE GLOBAL GW MOMENTUM FLUX BUDGET

Finally, Figure 11 contextualises my results by assessing the impact of TC-associated GWs on the atmosphere on a global scale. This is achieved by extrapolating from my satellite GW observations the full geophysical distribution of TCs.

I first produce an extended climatology of TCs, regardless of the available GW measurements. While IBTrACS data extend as far back as 1842, the great majority of observations

pre-date the satellite meteorological era and will thus be incomplete and inconsistent from year to year. Accordingly, I produce the climatology using the period 1978–2017 inclusive; this provides a forty-year time series for which the vast majority of TCs were measured during the satellite era (1979 to date). I assume any trend in the number or magnitude of TCs to be negligible over this period (e.g. Klotzbach, 2006).

For each observation in this period, I compute the SSHWS category and assign the median additional GW momentum flux associated with this category, as computed in section 6.1 above, to each individual observation. “Additional” here refers to the difference in medians between the “All” and “Background” distributions for each instrument in Figure 8, which I assume to be the additional contribution of TCs over background activity. This thus provides a first-order estimate for the additional momentum flux that would have been observed for each TC in the forty-year climatology if satellite GW data were available for the whole period.

Figure 11a–f shows the results of this analysis, subdivided by basin. For each panel, the horizontal axis shows the date within the annual cycle and the vertical axis shows the additional momentum flux associated with the TCs in that basin. Results for the South Atlantic basin have been omitted due to the very small number of data in IBTrACS describing TCs in this region.

The blue curve uses estimates from HIRDLS, the black curve from SABER and the red curve from MLS. Since inter-dataset differences are primarily in terms of momentum flux magnitude rather than the relative effect of each category of TC, the three datasets essentially show the same pattern, scaled slightly up or down. The horizontal dashed lines show the annual mean contribution due to TCs for each instrument; this is not a directly useful number for understanding TC

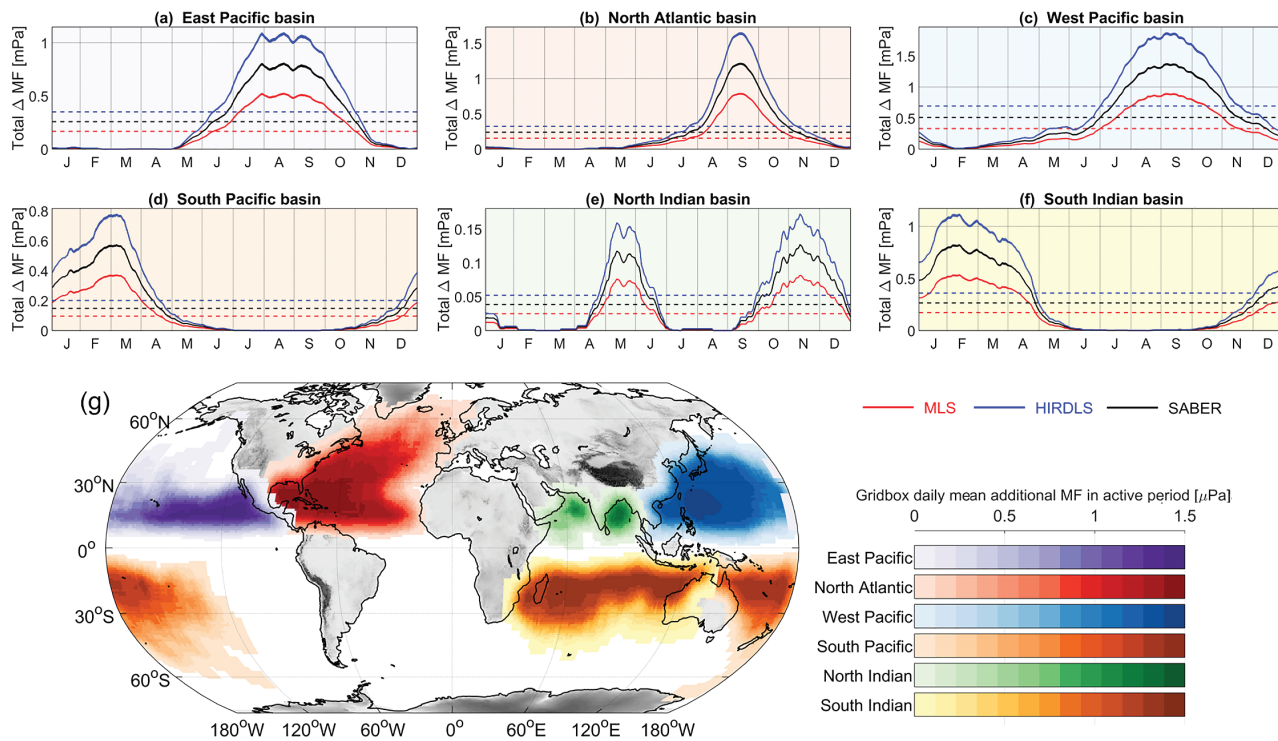


**FIGURE 11** Estimated contribution to the global momentum flux from TCs, computed using 1978–2017 TC climatology. (a–f) Annual cycle of additional TC-associated momentum flux, summed for each basin and each instrument separately. Dashed lines indicate the annual mean additional contribution. In each case, MLS is shown by the red (bottom) line, SABER the black (middle) line and HIRDLS the blue (top) line. (g) Map of mean momentum flux for additional (i.e. above-background) GWs associated with TCs, averaged over the “active season” (defined in the text). Note that values shown in panels (a–f) are basin-integral values in millipascals (mPa), while values in panel (g) are local values in micropascals ( $\mu$ Pa)

effects, but provides an approximate numerical estimate of the relative importance of TC-associated GWs to each basin at the annual level.

The additional momentum flux contributed by TCs is, for obvious reasons, mostly in regular TC seasons, that is, centred primarily in autumn in each hemisphere. Northern Hemisphere basins experience a larger effect than Southern Hemispheric basins, with only the South Indian basin in the Southern Hemisphere contributing basin-integral peak momentum fluxes as large as any of the Northern Hemispheric basins.

The basin that acts as the strongest source of TC-associated GWs is the West Pacific, with an annual mean of  $\sim 0.5$  mPa and a peak of  $\sim 1.9$  mPa. The East Pacific, North Atlantic and South Indian basins each contribute about half to two thirds this; for the East Pacific and South Indian basins this is a sustained contribution over around a third of the year, while for the North Atlantic basin the contribution is mostly delivered as a sharp peak between August and October. The South Pacific then provides around two thirds of the value of these three basins, while the North Indian basin contributes only a very small quantity of momentum fluxes, as two distinct seasonal peaks rather than one.

Figure 11g shows equivalent results spatially, using SABER estimates of additional momentum flux. SABER was chosen for this figure as it represents the median estimate in

every basin in Figure 11a–f. To compute the map, the additional momentum flux estimated for each TC in the forty-year climatology was first averaged for every day individually onto a  $1 \times 1^\circ$  global grid. An “active period” of the year was then identified for each basin, defined as all calendar days for which the all-years-average total additional momentum flux for that basin was above the annual mean additional momentum flux, that is to say, all days for which the black solid lines in Figure 11a–f lie above the black dashed lines. The additional momentum flux associated with each gridbox was then averaged over all active days in order to produce an estimate of the additional momentum flux due to TCs per gridbox per day during the TC season for each basin. Finally, the data were smoothed with a Gaussian smoother of 1,000 km full-width-at-half-maximum, to simulate the effects of the 1,000 km area used earlier to derive the additional momentum flux estimates. Note that the colour scales in Figure 11a–f show values in micropascals ( $\mu$ Pa), not millipascals (mPa) as in Figure 11a–f.

The largest daily increases in momentum flux during TC seasons are seen, unsurprisingly, in the main TC bands seen in Figure 1, centred around  $20 - 30^\circ$  off the Equator in both hemispheres. Particularly large peaks are seen in the Caribbean, between Japan and the Philippines, and extending eastwards and westwards from the northern coast of Australia. These regions contribute the majority of the

momentum flux total presented in Figure 11a–f and thus approach peak values of  $\sim 1$  mPa for a few weeks a year in the North Atlantic basin and a few months a year in the West Pacific and South Indian basins.

This is a small contribution relative to other GW sources, both locally and globally. Previous results for HIRDLS and SABER (e.g. Alexander *et al.*, 2008; Wright and Gille, 2011; Geller *et al.*, 2013; Ern *et al.*, 2018) suggest that, for the same season, altitude and geographic regions as the peaks in TC-associated GW activity, typical mean levels of momentum flux are  $\sim 0.5$  mPa over the whole of each region, compared to basin-total estimates of the same order for TCs. While some fraction of the GWs included in these reference averages will be from TCs, and even allowing for the possibility that the bulk of the time-mean TC-associated momentum flux is concentrated in short bursts with much higher local values, the additional momentum flux suggested by my results to be attributable to TCs specifically is small, and is thus very unlikely to be a major factor in the overall circulation. While the choice of a 1,000 km distance limit may lead to an underestimate of the full increase in GW activity in this spectral band associated with TCs, the difference due to this is not sufficiently large to provide the massive increase in momentum flux that would be needed to affect this overall conclusion (Figure 10).

Measured momentum flux values compare even more poorly to the dominant orographic sources of GWs such as the Andean tip, which has a mean July magnitude in HIRDLS observations of  $\sim 1$  mPa or greater and peak values at least an order of magnitude greater than this (Alexander *et al.*, 2008; Geller *et al.*, 2013; Wright *et al.*, 2016). Therefore, in the spectral range of the three instruments under consideration, I conclude that TCs make only a small contribution to the global GW momentum flux budget and hence to the overall middle- and upper-atmospheric circulation.

## 9 | SUMMARY AND CONCLUSIONS

Using a composite analysis method, I have characterised the properties of GWs associated with TCs using three satellite limb sounders. Using data derived from GW measurements closely associated with over 1,000 TCs, I see increases in GW temperature amplitudes and momentum fluxes over the TC centres, with activity rising steadily for the two weeks before the TC to a peak as the TC passes, before dramatically descending to background levels within significantly less than a day. This is consistent with previous research on longer vertical wavelength GWs (Hoffmann *et al.*, 2018), which suggested that GWs are most strongly associated with the intensification phase of TCs. GW effects remain enhanced for up to 4,000 km around the TC, suggesting the possibility of very long horizontal propagation distances (and consequently information transfer) for these waves; however, at least some

of this drop-off at large distance scales is likely to be due to the underlying distribution of “background” GW activity.

My results suggest that waves of smaller horizontal wave number may be generated during the intensification phase before the TC centre, but show no evidence of a change in vertical wave number. There is only a very weak dependence of any GW properties on TC intensity category, suggesting that the presence of the convective system is more important than how intense it is. However, I do see evidence of stronger GW activity over TCs that will later develop into Category 3 or higher hurricanes than those that will not; GWs over these “proto-hurricanes” have a median  $T'$  and  $MF$  15% higher than smaller TCs and 10% larger median values of  $k_z$  and  $k_h$ .

Finally, I show that TC-associated GWs of this type make only a very small contribution to the global GW momentum flux budget. Specifically, from my observations I extrapolate basin-total momentum flux peaks  $\sim 0.1$ – $1.6$  mPa. In the smaller subregions of the basins where the waves are primarily focused, and over the brief life cycle of an individual TC, this contribution may potentially be significant enough to briefly contribute a significant fraction of local time-mean values  $\sim 0.5$  mPa, but in the general case these GWs do not appear to have large enough effects to be of significance to the atmospheric circulation. This is consistent with previous case studies of individual cyclones (e.g. Jewtoukoff *et al.*, 2013), but I demonstrate here that this is also true when assessed over many thousands of such events and many hundreds of thousands of measurements.

Based on these results, I conclude that accurately modelling TC-generated GWs with short vertical and long horizontal wavelengths does not contribute significantly to the atmospheric circulation, and hence need not be a developmental priority for the next generation of weather and climate models. This is important because directly simulating such waves is highly computationally intensive and parameterising such waves is technically complex. Hence, an accurate representation of these waves would require significant computational expense, which may not be the best use of finite resources. However, there may be significant benefits in improving satellite GW observational capabilities: the stronger-than-typical GW activity associated with those TCs that later intensify into major hurricanes is a measurable effect that could be used to improve forecast lead times in the presence of heavy tropospheric cloud, with potential benefits for disaster planning and mitigation.

## ACKNOWLEDGEMENTS

I would like to thank John Gille (NCAR) for help in identifying a possible cloud-contamination issue with preliminary HIRDLS analyses, and all the relevant instrument teams and data centres for their work on collecting and processing the data used. I would also like to thank Nick Mitchell (Bath),

Peter Preusse (Fz. Juelich) and Lars Hoffmann (Fz. Juelich) for encouraging me to re-submit this article after rejection of an earlier version written in 2015, Dr Lars Hoffmann for useful comments on the earlier manuscript, and four anonymous reviewers across the two versions whose comments further improved the work. IBTrACS data were obtained from <http://www.ncdc.noaa.gov/ibtracs/>, HIRDLS and MLS data from <http://mirador.gsfc.nasa.gov/> and SABER data from <http://saber.gats-inc.com/> (all last accessed March 20, 2019).

## REFERENCES

- Alexander, M.J., Geller, M.A., McLandress, C., Polavarapu, S., Preusse, P., Sassi, F., Sato, K., Eckermann, S.D., Ern, M., Hertzog, A., Kawatani, Y., Pulido, M., Shaw, T.A., Sigmond, M., Vincent, R.A. and Watanabe, S. (2010) Recent developments in gravity-wave effects in climate models and the global distribution of gravity-wave momentum flux from observations and models. *Quarterly Journal of the Royal Meteorological Society*, 136, 1103–1124.
- Alexander, M.J., Gille, J.C., Cavanaugh, C.C., Coffey, M.T., Craig, C., Eden, T.D., Francis, G., Halvorson, C.M., Hannigan, J., Khosravi, R., Kinnison, D., Lee, H., Massie, S., Nardi, B., Barnett, J., Hepplewhite, C., Lambert, A., Dean, V., Eden, T.D., Francis, G., Halvorson, C.M., Hannigan, J., Khosravi, R., Kinneson, D., Lee, H., Massie, S., Nardi, B. and Lambert, A. (2008) Global estimates of gravity wave momentum flux from High Resolution Dynamics Limb Sounder observations. *Journal of Geophysical Research: Atmospheres*, 113, D15S18.
- Bushell, A.C., Butchart, N., Derbyshire, S.H., Jackson, D.R., Shutts, G.J., Vosper, S.B. and Webster, S. (2015) Parameterized gravity wave momentum fluxes from sources related to convection and large-scale precipitation processes in a global atmosphere model. *Journal of the Atmospheric Sciences*, 72, 4349–4371.
- de la Cámara, A., Lott, F. and Hertzog, A. (2014) Intermittency in a stochastic parameterization of nonorographic gravity waves. *Journal of Geophysical Research: Atmospheres*, 119, 11905–11919.
- Chane Ming, F., Chen, Z. and Roux, F. (2010) Analysis of gravity-waves produced by intense tropical cyclones. *Annales Geophysicae*, 28, 531–547.
- Chane Ming, F., Ibrahim, C., Barthe, C., Jolivet, S., Keckhut, P., Liou, Y.-A. and Kuleshov, Y. (2014) Observation and a numerical study of gravity waves during tropical cyclone Ivan (2008). *Atmospheric Chemistry and Physics*, 14, 641–658.
- Chen, D., Chen, Z. and Lü, D. (2012) Simulation of the stratospheric gravity waves generated by the Typhoon Matsa in 2005. *Science China Earth Sciences*, 55, 602–610.
- Das, S.S., Uma, K.N. and Das, S.K. (2012) MST radar observations of short-period gravity wave during overhead tropical cyclone. *Radio Science*, 47, RS2019.
- Dhaka, S.K. (2003) Gravity wave generation in the lower stratosphere due to passage of the typhoon 9426 (Orchid) observed by the MU radar at Shigaraki (34.85°N, 136.10°E). *Journal of Geophysical Research: Atmospheres*, 108, 4595.
- Eckermann, S.D. (2011) Explicitly stochastic parameterization of nonorographic gravity wave drag. *Journal of the Atmospheric Sciences*, 68, 1749–1765.
- Efron, B. (1979) Bootstrap methods: another look at the Jackknife. *The Annals of Statistics*, 7, 1–26.
- Ern, M., Preusse, P., Alexander, M.J. and Warner, C.D. (2004) Absolute values of gravity wave momentum flux derived from satellite data. *Journal of Geophysical Research: Atmospheres*, 109, D20103.
- Ern, M., Preusse, P., Gille, J.C., Hepplewhite, C.L., Mlynaczak, M.G., Russell, J.M. and Riese, M. (2011) Implications for atmospheric dynamics derived from global observations of gravity wave momentum flux in stratosphere and mesosphere. *Journal of Geophysical Research*, 116, D19107.
- Ern, M., Trinh, Q.T., Preusse, P., Gille, J.C., Mlynaczak, M.G., Russell, I., J.M. and Riese, M. (2018) GRACILE: a comprehensive climatology of atmospheric gravity wave parameters based on satellite limb soundings. *Earth System Science Data*, 10, 857–892.
- Fritts, D.C. and Alexander, M.J. (2003) Gravity wave dynamics and effects in the middle atmosphere. *Reviews of Geophysics*, 41. <https://doi.org/10.1029/2001RG000106>.
- Geller, M.A., Alexander, M.J., Love, P.T., Bacmeister, J.T., Ern, M., Hertzog, A., Manzini, E., Preusse, P., Sato, K., Scaife, A.A. and Zhou, T. (2013) A comparison between gravity wave momentum fluxes in observations and climate models. *Journal of Climate*, 26, 6383–6405.
- Gille, J.C., Gray, L.J., Cavanaugh, C.C., Coffey, M.T., Dean, V., Halvorson, C.M., Karol, S., Khosravi, R., Kinnison, D.E., Massie, S.T., Nardi, B., Belmonte Rivas, M., Smith, L., Torpy, B., Waterfall, A., Wright, C.J., Choi, K.Y., Craig, C. and Hepplewhite, C.L. (2013) *High Resolution Dynamics Limb Sounder Earth Observing System Data Description and Quality, Version 7*. Technical report from NASA.
- Guan, W. (2003) From the help desk: bootstrapped standard errors. *The Stata Journal*, 3, 71–80.
- Hecht, J.H., Alexander, M.J., Walterscheid, R.L., Gelinas, L.J., Vincent, R.A., MacKinnon, A.D., Woithe, J.M., May, P.T., Skinner, W.R., Mlynaczak, M.G. and Russell, J.M. (2009) Imaging of atmospheric gravity waves in the stratosphere and upper mesosphere using satellite and ground-based observations over Australia during the TWPICE campaign. *Journal of Geophysical Research: Atmospheres*, 114, D18123.
- Hertzog, A., Alexander, M.J. and Plougonven, R. (2012) On the intermittency of gravity-wave momentum flux in the stratosphere. *Journal of the Atmospheric Sciences*, 69, 3433–3448.
- Hoffmann, L., Wu, X. and Alexander, M.J. (2018) Satellite observations of stratospheric gravity waves associated with the intensification of tropical cyclones. *Geophysical Research Letters*, 45, 1692–1700.
- Jewtoukoff, V., Plougonven, R. and Hertzog, A. (2013) Gravity waves generated by deep tropical convection: estimates from balloon observations and mesoscale simulations. *Journal of Geophysical Research: Atmospheres*, 118, 9690–9707.
- Kim, S.H., Chun, H.-Y. and Jang, W. (2014) Horizontal divergence of typhoon-generated gravity waves in the upper troposphere and lower stratosphere (UTLS) and its influence on typhoon evolution. *Atmospheric Chemistry and Physics*, 14, 3175–3182.
- Kim, S.Y., Chun, H.Y. and Wu, D.L. (2009) A study on stratospheric gravity waves generated by Typhoon Ewiniar: numerical simulations and satellite observations. *Journal of Geophysical Research: Atmospheres*, 114, D22104.
- Kim, Y.-H., Bushell, A.C., Jackson, D.R. and Chun, H.-Y. (2013) Impacts of introducing a convective gravity-wave parameterization upon the QBO in the Met Office Unified Model. *Geophysical Research Letters*, 40, 1873–1877.
- Klotzbach, P.J. (2006) Trends in global tropical cyclone activity over the past twenty years (1986–2005). *Geophysical Research Letters*, 33, L10805.

- Knapp, K.R., Kruk, M.C., Levinson, D.H., Diamond, H.J. and Neumann, C.J. (2010) The International Best Track Archive for Climate Stewardship (IBTrACS): unifying tropical cyclone data. *Bulletin of the American Meteorological Society*, 91, 363–376.
- Kuester, M.A., Alexander, M.J. and Ray, E.A. (2008) A model study of gravity waves over Hurricane Humberto (2001). *Journal of the Atmospheric Sciences*, 65, 3231–3246.
- Livesey, N.J., Read, W.G., Wagner, P.A., Froidevaux, L., Lambert, A., Manney, G.L., Millán Valle, L., Pumphrey, H.C., Santee, M.L., Schwartz, M.J., Wang, S., Fuller, R.A., Jarnot, R.F., Knosp, B.W. and Martinez, E. (2015) Earth Observing System (EOS) Aura Microwave Limb Sounder (MLS) Data Quality and Description. Technical report from NASA, version 4.2.
- Lott, F., Guez, L. and Maury, P. (2012) A stochastic parameterization of non-orographic gravity waves: formalism and impact on the equatorial stratosphere. *Geophysical Research Letters*, 39, L06807.
- Nastrom, G.D. and Gage, K.S. (1985) A climatology of atmospheric wavenumber spectra of wind and temperature observed by commercial aircraft. *Journal of the Atmospheric Sciences*, 42, 950–960.
- Niranjan Kumar, K., Ramkumar, T. and Krishnaiah, M. (2011) MST radar observation of inertia-gravity waves generated from tropical cyclones. *Journal of Atmospheric and Solar-Terrestrial Physics*, 73, 1890–1906.
- Niranjan Kumar, K., Rao, C.K., Sandeep, A. and Rao, T.N. (2014) SODAR observations of inertia-gravity waves in the atmospheric boundary layer during the passage of tropical cyclone. *Atmospheric Science Letters*, 15, 120–126.
- Pfister, L., Chan, K.R., Bui, T.P., Bowen, S., Legg, M., Gary, B., Kelly, K., Proffitt, M. and Starr, W. (1993) Gravity waves generated by a tropical cyclone during the STEP tropical field program: a case study. *Journal of Geophysical Research: Atmospheres*, 98, 8611–8638.
- Plougonven, R. and Zhang, F. (2014) Internal gravity waves from atmospheric jets and fronts. *Reviews of Geophysics*, 52, 33–76.
- Remsberg, E.E., Marshall, B.T., Garcia-Comas, M., Krueger, D., Lin-genfelser, G.S., Martin-Torres, J., Mlynaczak, M.G., Russell, J.M., Smith, A.K., Zhao, Y., Brown, C., Gordley, L.L., Lopez-Gonzalez, M.J., Lopez-Puertas, M., She, C.-Y., Taylor, M.J. and Thompson, R.E. (2008) Assessment of the quality of the Version 1.07 temperature-versus-pressure profiles of the middle atmosphere from TIMED/SABER. *Journal of Geophysical Research: Atmospheres*, 113, D17101.
- Sato, K. (1993) Small-scale wind disturbances observed by the MU radar during the passage of Typhoon Kelly. *Journal of the Atmospheric Sciences*, 50, 518–537.
- Stockwell, R.G., Mansinha, L. and Lowe, R. (1996) Localization of the complex spectrum: the S transform. *IEEE Transactions on Signal Processing*, 44, 998–1001.
- Tang, X.-D., Yang, M.-J. and Tan, Z.-M. (2012) A modeling study of orographic convection and mountain waves in the landfalling typhoon Nari (2001). *Quarterly Journal of the Royal Meteorological Society*, 138, 419–438.
- Tsuda, T., Murayama, Y., Wiryo Sumarto, H., Harijono, S.W.B. and Kato, S. (1994) Radiosonde observations of equatorial atmosphere dynam-ics over Indonesia: 2. Characteristics of gravity waves. *Journal of Geophysical Research: Atmospheres*, 99, 10507–10516.
- Wright, C.J. (2010) *Detection of stratospheric gravity waves using HIRDLS data*. DPhil thesis, Oxford University.
- Wright, C.J., Belmonte Rivas, M. and Gille, J.C. (2011) Intercomparisons of HIRDLS, COSMIC and SABER for the detection of stratospheric gravity waves. *Atmospheric Measurement Techniques*, 4, 1581–1591.
- Wright, C.J. and Gille, J.C. (2011) HIRDLS observations of gravity wave momentum fluxes over the monsoon regions. *Journal of Geophysical Research: Atmospheres*, 116, D12103.
- Wright, C.J. and Gille, J.C. (2013) Detecting overlapping gravity waves using the S-Transform. *Geophysical Research Letters*, 40, 1850–1855.
- Wright, C.J. and Hindley, N.P. (2018) How well do stratospheric reanalyses reproduce high-resolution satellite temperature measurements?. *Atmospheric Chemistry and Physics*, 18, 13703–13731.
- Wright, C.J., Hindley, N.P., Hoffmann, L., Alexander, M.J. and Mitchell, N.J. (2017) Exploring gravity wave characteristics in 3-D using a novel S-transform technique: AIRS/Aqua measurements over the Southern Andes and Drake Passage. *Atmospheric Chemistry and Physics*, 17, 8553–8575.
- Wright, C.J., Hindley, N.P., Moss, A.C. and Mitchell, N.J. (2016) Multi-instrument gravity-wave measurements over Tierra del Fuego and the Drake Passage - part 1: potential energies and vertical wavelengths from AIRS, COSMIC, HIRDLS, MLS-Aura, SAAMER, SABER and radiosondes. *Atmospheric Measurement Techniques*, 9, 877–908.
- Wright, C.J., Osprey, S.M. and Gille, J.C. (2013) Global observations of gravity wave intermittency and its impact on the observed momentum flux morphology. *Journal of Geophysical Research: Atmospheres*, 118, 10980–10993.
- Wright, C.J., Osprey, S.M. and Gille, J.C. (2015) Global distributions of overlapping gravity waves in HIRDLS data. *Atmospheric Chemistry and Physics*, 15, 4333–4382.
- Wu, D.L. and Zhang, F. (2004) A study of mesoscale gravity waves over the North Atlantic with satellite observations and a mesoscale model. *Journal of Geophysical Research: Atmospheres*, 109, D22104.
- Yue, J., Miller, S.D., Hoffmann, L. and Straka, W.C. (2014) Stratospheric and mesospheric concentric gravity waves over tropical cyclone Mahasen: joint AIRS and VIIRS satellite observations. *Journal of Atmospheric and Solar-Terrestrial Physics*, 119, 83–90.

**How to cite this article:** Wright CJ. Quantifying the global impact of tropical cyclone-associated gravity waves using HIRDLS, MLS, SABER and IBTrACS data. *QJR Meteorol Soc.* 2019;145:3023–3039.

<https://doi.org/10.1002/qj.3602>